

## Article

# Functionalized Carbon-Nanotubes-Based Thin-Film Transistor Sensor for Highly Selective Detection of Methane at Room Temperature

Feifan Ji <sup>1,2</sup>, Jinyong Hu <sup>1,\*</sup> and Yong Zhang <sup>1,2,\*</sup> <sup>1</sup> School of Physics and Optoelectronics, Xiangtan University, Xiangtan 411105, China; jff\_274@163.com<sup>2</sup> Hunan Institute of Advanced Sensing and Information Technology, Xiangtan University, Xiangtan 411105, China

\* Correspondence: jyhu\_233@xtu.edu.cn (J.H.); zhangyong@xtu.edu.cn (Y.Z.)

**Abstract:** Gas sensors based on carbon nanotubes (CNTs) as channel materials have been widely considered as promising candidates for the detection of toxic gas. However, effectively detecting methane (CH<sub>4</sub>) with CNTs-based sensors remains challenging because nonpolar CH<sub>4</sub> molecules find it difficult to directly interact with CNTs. Herein, a functionalized CNTs-based thin-film transistor (TFT) sensor is proposed for the highly effective detection of CH<sub>4</sub> at room temperature, where CNTs with high semiconductor purity are used as the main TFT channel. The VO<sub>2</sub> and Pd nanoparticles serve as surface-active agents to modify the CNTs, and the surface-modified CNTs-based gas sensor exhibits excellent gas-sensing properties for the detection of CH<sub>4</sub>. In particular, the Pd@VO<sub>2</sub> composite-modified CNTs-based TFT sensor has excellent sensitivity to CH<sub>4</sub> in the detection range of 50 to 500 ppm. The detection limit is as low as 50 ppm, and the sensor exhibits excellent selectivity and superior repeatability. The improved gas-sensing properties of the CNTs-based gas sensor is primarily attributed to the modification of the sensitive channel that can promote the electronic interaction between CH<sub>4</sub> and gas-sensing materials. This study provides guidance for the development of high-performance CH<sub>4</sub> sensors operating at room temperature.

**Keywords:** gas sensors; CNTs-based sensor; functionalized CNTs; CH<sub>4</sub> sensor; Pd nanoparticle modification



**Citation:** Ji, F.; Hu, J.; Zhang, Y. Functionalized Carbon-Nanotubes-Based Thin-Film Transistor Sensor for Highly Selective Detection of Methane at Room Temperature.

*Chemosensors* **2023**, *11*, 365.

<https://doi.org/10.3390/chemosensors11070365>

Academic Editor: Andrea Ponzoni

Received: 2 May 2023

Revised: 17 June 2023

Accepted: 20 June 2023

Published: 29 June 2023



**Copyright:** © 2023 by the authors. Licensee MDPI, Basel, Switzerland. This article is an open access article distributed under the terms and conditions of the Creative Commons Attribution (CC BY) license (<https://creativecommons.org/licenses/by/4.0/>).

## 1. Introduction

As a common flammable and explosive gas, methane (CH<sub>4</sub>) not only causes explosions in coal mining operations but also leads to climate change as an infrared radiation absorber in the atmosphere [1–3]. Therefore, the effective detection of CH<sub>4</sub> in our modern society is crucial. Currently, resistive metal–oxide semiconductor (MOS) gas sensors have been widely applied for the detection of hazardous gases [4–7]. In general, MOS gas sensors usually requires a relatively high operating temperature to provide sufficient reaction activation energy to achieve effective detection of gas molecules [8,9]. However, such gas sensors operating at high temperatures usually require higher power to maintain their operation [10], and the high energy consumption is a challenge for the endurance of personal gas sensors. Therefore, there is an urgent need to develop a gas sensor that works at low temperatures or even at room temperature to achieve the low-power detection of CH<sub>4</sub> gas.

In recent years, carbon nanotubes (CNTs) have been widely used as sensing materials for gas detection at room temperature due to their effective charge transfer with gas molecules at this temperature [11,12]. CNTs-based sensors are promising candidates for the highly sensitive detection of CH<sub>4</sub> gas at room temperature [13,14]. For instance, the CNT thin-film sensors prepared by Shano et al. via the chemical deposition method were highly sensitive to CH<sub>4</sub> and other gases [13]. Although CNTs-based sensors can

detect CH<sub>4</sub> at room temperature, the selectivity of CH<sub>4</sub> to CNTs in the original state is unsatisfactory because nonpolar CH<sub>4</sub> molecules do not easily electronically interact with pristine CNTs [15,16]. Prashant Shukla et al. used functionalized CNTs to make a sensor that can detect CH<sub>4</sub> at room temperature with high selectivity and repeatability [14]. Therefore, in order to increase the selectivity to CH<sub>4</sub> and reduce the cross-sensitivity to other interfering gases, the reasonable functional modification of CNTs is a promising strategy [17–19]. Studies have shown that nanocomposites provide high-performance gas detection [20]: VO<sub>2</sub> can be sensitive to CH<sub>4</sub> [21,22], and noble Pd has a favorable catalytic effect on CH<sub>4</sub> [23–25]. In addition, due to the transconductance of field-effect transistor (FET) sensors, the gas sensors based on the FET structure have a strong amplification effect of weak signals and can realize the detection of lower concentrations of gas molecules with high sensitivity [26–28]. Therefore, they are expected to achieve the high-selectivity, low-concentration, and high-sensitivity detection of CH<sub>4</sub> at room temperature via modifying CNTs and the construction of FET gas sensors.

Inspired by the above considerations, in this work, a functionalized CNTs-based thin-film transistor (TFT) sensor was developed for the effective detection of CH<sub>4</sub>, where CNTs are used as the conductive channel of the TFT, and the surface-modified Pd@VO<sub>2</sub> composite is used as the sensitive layer of sensors to capture the CH<sub>4</sub> molecules. The gas-sensing properties of the functionalized CNTs-based TFT sensor were investigated in detail, and the enhancement mechanism of gas-sensing properties was also theoretically analyzed. It is expected that this method will provide useful guidance for improving the gas-sensing properties of CNTs-based CH<sub>4</sub> gas sensors.

## 2. Materials and Methods

The CNTs with a semiconductor purity higher than 99.9% used in this study were provided by Peking University, and the specific experimental steps can be found in other reported studies [29,30]. The CNTs-based TFT and sensitive materials were prepared via advanced semiconductor techniques, including laser direct-writing lithography (Microwriter ML<sup>®</sup>3, Durham Magneto Optics Ltd., Cambridge, UK), reactive ion etching (Haasrode-R200A, Jiangsu Leuven Instruments Co., Ltd., Xuzhou, China), a DMP-2850 inkjet printer (Su Zhou Hizenith Robot Co., Ltd., Suzhou, China), and electron beam evaporation (DE400, Beijing DE Technology Inc., Beijing, China). Figure 1a illustrates the well-designed fabrication process of CNTs-based TFT gas sensors. Briefly, the drain and source were first defined via photolithography, and Ti/Pd/Au (0.6 nm/20 nm/40 nm) were then deposited via electron beam evaporation. Subsequently, the redundant CNTs were removed via reactive ion etching (RIE) under an oxygen environment to form a channel 300 μm in length and 600 μm in width. After that, 5 wt % VO<sub>2</sub> nanoparticle ink was prepared. The VO<sub>2</sub> ink contained VO<sub>2</sub> nanoparticles as the solute and isopropanol (10 mL) and ethylene glycol propyl ether (10 mL) as the solvent. BYK-190 and BYK-346 were added to the ink so that the VO<sub>2</sub> nanoparticles were uniformly dispersed in the solvent, and the viscosity of the solution was adjusted to match the conditions required for inkjet printing. Then, the prepared solution was magnetically stirred at room temperature (25 °C) for 12 h to obtain the VO<sub>2</sub> nanoparticle ink (viscosity: 4.3 mPas). After filling the VO<sub>2</sub> ink into the configured ink box, inkjet deposition was performed on the channel defined by the photolithography, and then the sensor was placed in an oven at 200 °C under a vacuum for 30 min to remove the other impurities outside the VO<sub>2</sub> particles. Finally, Pd (1 nm) was modified on VO<sub>2</sub> via electron beam evaporation. In this work, except for the VO<sub>2</sub> nanoparticles (size: 100–200 nm, Hongwu Material Technology Co., Ltd., Guangzhou, China), all the chemical reagents used for ink configuration were purchased from Aladdin Biochemical Technology Co., Ltd. (Shanghai, China), without further purification.

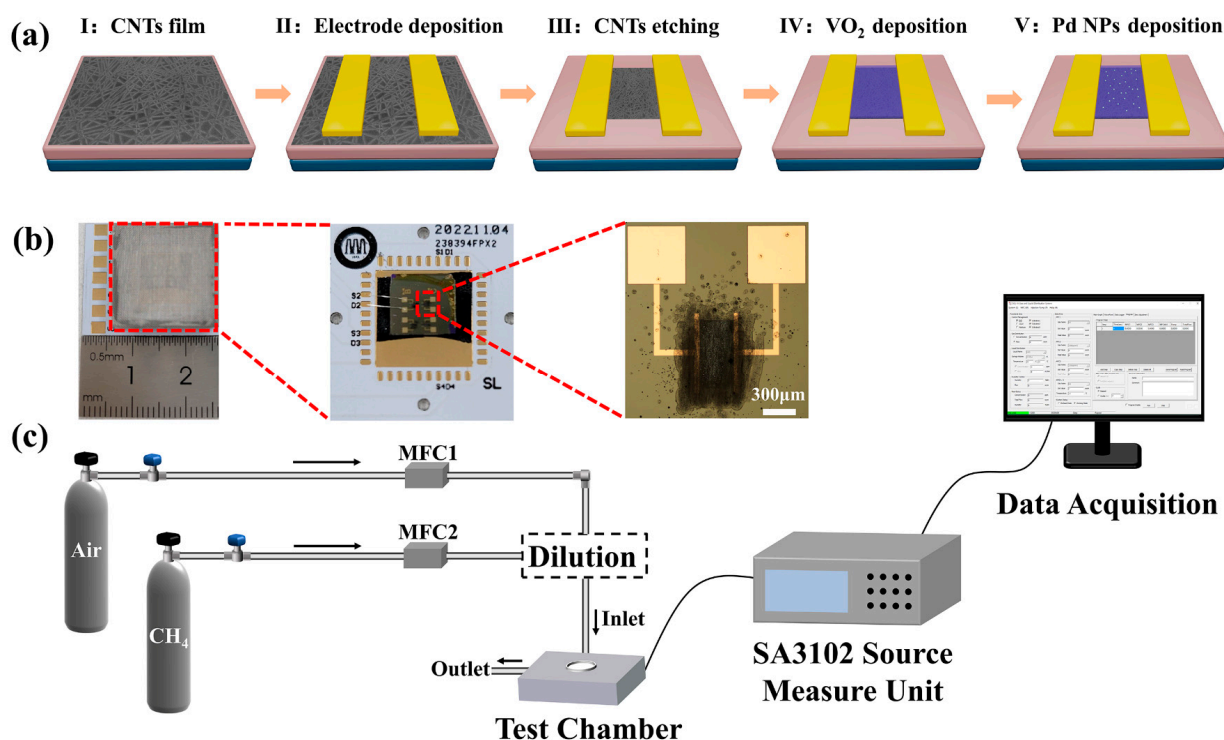


**Figure 1.** (a) Fabrication process flow diagram, (b) a typically fabricated chip, and (c) schematic diagram of the gas-sensing measurement setup.

The morphologies of the CNTs and VO<sub>2</sub> films were observed via field-emission scanning electron microscopy (FE-SEM, Sigma500, ZEISS, Oberkochen, Germany). The purity of the CNTs film was studied with a UV–vis–NIR spectrophotometer (UV-3600, Shimadzu, Kyoto, Japan). The defect degree of the CNT film and the molecular structure of the Pd@VO<sub>2</sub> material were studied via Raman spectroscopy (Renishaw, Wotton-under-Edge, UK). The chemical composition of the material was characterized via energy-dispersive X-ray spectroscopy (EDS). The composition of VO<sub>2</sub> was analyzed via X-ray diffraction (XRD, Rigaku D/Max 2500 PC, Bruker, Mannheim, Germany). The surface composition and chemical state were studied via X-ray photoelectron spectroscopy (XPS, Thermo escalab 250 Xi, Thermo Fisher Scientific, Waltham, MA, USA) using an Al K $\alpha$  excitation source. The electrical properties of the CNTs-based TFT were measured using a Keithly 4200 semiconductor analyzer and a probe station (Cascade Microtech MPS 150, Tektronix, Beaverton, OR, USA). In order to measure the gas-sensing properties, the as-prepared sensor was assembled on a self-made PCB board via wire bonding, as shown in Figure 1b. The performance of the gas sensor was measured on a CGS-MT intelligent gas sensitivity analysis system (Beijing Elite Technology Co., Ltd., Beijing, China), as shown in Figure 1c. Usually, sensitivity is defined as the ratio of sensor response to gas concentration [31]. The response can be defined as  $(I_a - I_g)/I_a \times 100(\%)$ , where  $I_a$  and  $I_g$  are the current of the sensor in air and the target gas, respectively [32].

### 3. Results and Discussion

TFT-type sensors take advantage of CNTs as the channel material and then utilize Pd@VO<sub>2</sub>-modified CNTs as the sensitive material to capture CH<sub>4</sub>. Therefore, high-semiconductor purity CNT films and pure Pd@VO<sub>2</sub> materials without other impurities are the fundamental guarantee for realizing the sensitive detection of CH<sub>4</sub> [29,30]. In order to study the morphology, purity, and defects of the CNT film, FE-SEM images, UV–vis–NIR absorption spectra, and Raman spectra are obtained. The SEM image in Figure S1 shows a randomly oriented and uniform CNT film [33], which laid the foundation for the fabrication of a TFT gas sensor with high sensitivity [10]. Figure 2a shows the absorption spectra of

the CNT film in the range of 400–1500 nm. The existence of the M11 peak (located between 600 and 800 nm) and the sharp S22 peak (located at 820–1350 nm) indicates that the CNT film had with high semiconductor purity, which is a prerequisite to ensure the successful preparation of CNTs-based FET sensors [26]. According to the experimental relationship of  $\omega = 248/d$  (nm), the radial breathing mode (RBM) peak (Figure 2b) at  $168 \text{ cm}^{-1}$  indicated that the diameter of the CNTs was distributed around 1.5 nm [10]. The high  $I_G/I_D$  ratio indicated that the CNTs used in this work exhibited fewer defects, which explained the subsequent modification of the CNTs film. In addition, the symmetrical Lorentz-type G peak indicated the semiconductor nature of the CNTs, which is consistent with the results obtained via absorption spectrum (Figure 2a). In order to determine the distribution and composition of the VO<sub>2</sub> and Pd materials, FE-SEM images, EDS spectra, XRD patterns, Raman spectra, and XPS spectra were obtained. Figure S2 depicts an SEM image of Pd@VO<sub>2</sub>, and the inset shows an FE-SEM image at high magnification. It can be seen that the material produced via inkjet printing had a more uniform distribution, which is conducive to the uniform diffusion of gas molecules on the surface [34]. At high magnification, the diameter of the VO<sub>2</sub> nanoparticles could be estimated to be about 100–200 nm, but the Pd nanoparticles could not be well observed in the SEM image due to their small amount. In order to verify the presence of Pd nanoparticles, EDS analysis was carried out. In addition to the V and O, Si could be seen in the EDS spectrum; Pd could also be observed, as shown in Figure 2c, which confirmed the existence of Pd in the Pd@VO<sub>2</sub> composites [35]. The spectrum shows that there were no other impurities in the sample (the Si element's peak originated from the silicon substrate). The EDS mapping in Figure S3a–c also shows the uniform element distribution in each part of the material, which is consistent with the above SEM results. Figure 2d shows the XRD spectra of the Pd@VO<sub>2</sub> and VO<sub>2</sub> materials. It can be seen that there was no change after Pd modification, and all the diffraction peaks in the XRD spectra corresponded to monoclinic VO<sub>2</sub> (PDF#44-0252) [36,37]. No other phase or impurity peaks were detected in the XRD spectra, further indicating the high purity of the material prepared in this work. In order to investigate the molecular structure of the as-prepared material, the Raman spectra of VO<sub>2</sub> and Pd@VO<sub>2</sub> were measured, as depicted in Figure 2e. It can be seen that there was no change in the Raman spectrum of VO<sub>2</sub> after the modification with Pd nanoparticles. The five peaks at  $140 \text{ cm}^{-1}$ ,  $282 \text{ cm}^{-1}$ ,  $408 \text{ cm}^{-1}$ ,  $691$ , and  $991 \text{ cm}^{-1}$  correspond to the fundamental modes of VO<sub>2</sub> monoclinic crystal, which is consistent with the results of XRD patterns. The two peaks at  $140 \text{ cm}^{-1}$  and  $187 \text{ cm}^{-1}$  are strongly consistent with a layered structure. The other peaks at  $282 \text{ cm}^{-1}$  and  $408 \text{ cm}^{-1}$  are the bending vibration bonds of V=O. The peak at  $691 \text{ cm}^{-1}$  conforms to the double oxygen (V-O-V) stretching mode, which is formed by the sharing of oxygen at the corners of two pyramids. The high long-shift peak at  $991 \text{ cm}^{-1}$  is consistent with the tensile vibration of terminal oxygen (V=O) [38–40]. The surface chemical state of Pd@VO<sub>2</sub> was further determined via XPS measurements. The XPS spectra in Figure 2f prove the presence of V, O, and Pd elements, and the C 1s peak was used for charge correction [41]. The O 1s peak ( $\sim 530.2 \text{ eV}$ ) and Pd 3p<sub>3/2</sub> peak ( $532.9 \text{ eV}$ ) can be observed from Figure 2g. The Pd 3p<sub>3/2</sub> peak, Pd 3d<sub>3/2</sub> peak ( $341.5 \text{ eV}$ ), and Pd 3d<sub>5/2</sub> peak ( $336.2 \text{ eV}$ ) in Figure 2i proved that the existence of Pd in the form of an elementary substance [42], which guaranteed the catalytic effect during the subsequent gas-sensing reaction. In the spectra in Figure 2h, the two binding energies of  $517 \text{ eV}$  and  $515.9 \text{ eV}$  obtained in the V 2p<sub>3/2</sub> environment belong to V<sup>5+</sup> and V<sup>4+</sup>, respectively. The large amount of V<sup>5+</sup> may have been due to the easy oxidation of vanadium in contact with air during the gas-sensing test, so completely oxidized V<sup>5+</sup> seems to be very common on the surface of vanadium-oxide materials [43].

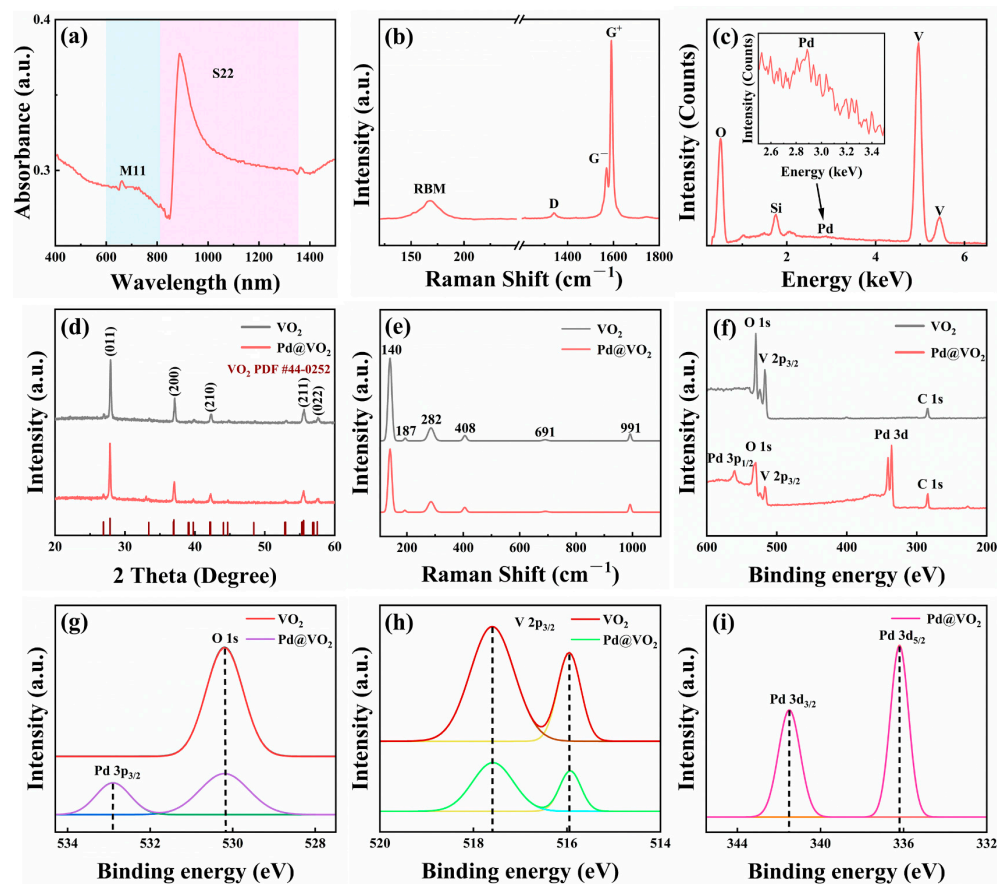


**Figure 2.** Characterization of the CNTs, VO<sub>2</sub>, and Pd@VO<sub>2</sub> thin film used for constructing gas sensors. The (a) UV–vis–NIR absorption spectrum and the (b) Raman spectrum of the CNT film. (c) EDS, (d) XRD patterns, (e) Raman spectra, and (f) XPS full spectra of VO<sub>2</sub> and Pd@VO<sub>2</sub>. (g–i) Fine spectra obtained by narrow area scanning of Pd@VO<sub>2</sub>.

As a platform utilized for the detection of CH<sub>4</sub>, CNTs-based TFT sensors should be reliable and uniform. CNTs-based TFT sensors were tested using a common source approach with gate voltages ranging from  $-60$  V to  $+60$  V and a fixed drain-source voltage of  $-0.1$  V. The randomly selected unmodified CNTs-based TFT sensors exhibited highly uniform transfer characteristic curves with small changes (Figure 3a). All transistors exhibited p-type FET characteristics [44], and the current on/off ratio was calculated to be greater than  $10^4$ , which is crucial for charge transport and reliable detection. In order to compare the effect of VO<sub>2</sub>, Pd, and Pd@VO<sub>2</sub> modification, the corresponding transfer characteristic curves of the modified CNTs-based TFT sensors were also tested (Figure 3b). Compared with the unmodified TFT, the VO<sub>2</sub> material deposited on TFT did not change the transfer characteristic curve. However, the threshold voltage of CNTs modified with Pd generated significant drift due to the strong shielding effect of Pd nanoparticles [12]. For the Pd@VO<sub>2</sub> TFT sensor, the transfer characteristic curve of TFT showed a significant horizontal shift, which was caused by the change in the work function of the sensitive materials [45]. The gas-sensing properties of CNTs-based TFT sensors modified with VO<sub>2</sub> and Pd@VO<sub>2</sub> were further investigated. All the sensing measurements in this work were recorded at  $V_{ds} = -0.1$  V and  $V_{gs-backgate} = 0$  V, working at room temperature. In order to explore the optimal temperature of the sensor, the Pd@VO<sub>2</sub> TFT sensor was measured at different temperatures from room temperature ( $25$  °C) to  $100$  °C. It can be seen from Figure 4a that the Pd@VO<sub>2</sub> TFT sensor demonstrated the strongest response at room temperature. With the increase in temperature, VO<sub>2</sub> is oxidized to V<sub>2</sub>O<sub>3</sub> and V<sub>2</sub>O<sub>5</sub>, which leads to the decrease in the response of the sensor [46]. Figure 4b shows the transient response of the CNTs-based sensors modified with VO<sub>2</sub> and Pd@VO<sub>2</sub> to 50–500 ppm CH<sub>4</sub>

at room temperature. It can be clearly observed that the response of the Pd@VO<sub>2</sub> TFT sensor increased sharply when CH<sub>4</sub> was introduced, while the VO<sub>2</sub> TFT sensor had almost no response to CH<sub>4</sub> in the concentration range from 50 to 200 ppm. Noticeably, the TFT sensors presented comparatively regular baseline drift during the gas-sensing test cycles. Baseline drift is typical for the metal-oxide-based gas sensors, which is normally attributed to surface atomic rearrangement [47]. Additionally, the regular baseline drift seems to be an inevitable phenomenon for Pd@VO<sub>2</sub> TFT gas sensors, which can be handled by the back-end circuit in future practical applications. Because the response reflects the relative change in current, the baseline drift has relatively little interference on gas-sensing detection. Figure S4 shows the two-cycle response–recovery curve of the Pd-modified CNT sensor toward 500 ppm CH<sub>4</sub>. After CH<sub>4</sub> was introduced, the current of the sensor did not change, indicating that the Pd modified CNTs-based sensor was not sensitive to CH<sub>4</sub>. This further confirmed that Pd only plays a catalytic role in the sensor. Figure 4c plots the fitting curves of the VO<sub>2</sub> TFT sensor and Pd@VO<sub>2</sub> TFT sensor at the CH<sub>4</sub> test concentration. It can be seen that the experimental limits of detection (LODs) of the VO<sub>2</sub> TFT sensor and Pd@VO<sub>2</sub> TFT sensor were 300 ppm and 50 ppm, respectively. According to the theoretical calculation formula ( $LOD \text{ (ppm)} = 3 \times RMS_{noise} / Slope$ ) [48], Pd@VO<sub>2</sub> and VO<sub>2</sub> TFT sensors can achieve detection limits of 25 ppm and 195 ppm, respectively. Moreover, the sensitivities of the Pd@VO<sub>2</sub> and VO<sub>2</sub> TFT sensors were calculated to be 0.698% ppm<sup>-1</sup> and 0.273% ppm<sup>-1</sup>, respectively. Therefore, Pd modification not only improves the detection limit of the sensor for CH<sub>4</sub> but also improve the sensitivity. Figure 4d depicts the dynamic response of the sensor to 500 ppm CH<sub>4</sub> working at room temperature. After the sensor was exposed to 500 ppm CH<sub>4</sub> for 30 min to record the sensing signal, the sensor was exposed to a clean air flow for 30 min again to recover the sensor, and four such cycles were repeated. The incomplete recyclability could be ascribed to the fact that the desorption energy required for gas desorption is difficult to be satisfied at room temperature. The sensing behavior of the VO<sub>2</sub> and Pd@VO<sub>2</sub> TFT sensors seemed to be quite repeatable. It can also be clearly seen from Figure 4e that the Pd@VO<sub>2</sub> TFT sensor had a stronger response to CH<sub>4</sub> than the VO<sub>2</sub> TFT sensor. From the responses of the two sensors to CH<sub>4</sub> shown in Figure 4e, it could be calculated that the response of Pd@VO<sub>2</sub> TFT sensor was about five times than that of the VO<sub>2</sub> TFT sensor. This enhancement could be attributed to the Pd nanoparticles catalyzing the dissociation and adsorption of CH<sub>4</sub> and oxygen molecules via the spillover effect [2], which then facilitates the adsorption of CH<sub>4</sub> and increases the electronic interaction with CNTs, which leads to the reduction in CNTs carriers and makes the sensor more responsive. In addition, the selectivity of a gas sensor is an important parameter in practical applications. The selectivity of the Pd@VO<sub>2</sub> TFT sensor to CH<sub>4</sub> was compared by contacting different gases of SO<sub>2</sub>, CO, benzene, and CH<sub>4</sub>, which are common gases in coal mines and kitchens. Figure 4e shows the selectivity histogram of the Pd@VO<sub>2</sub> TFT sensor at room temperature, and the selectivity to a specific gas is defined as  $S_{specific \text{ gas}} / S_{interference \text{ gas}}$  [49]. Compared with CH<sub>4</sub>, the selectivity to SO<sub>2</sub>, CO, and benzene was about 49%, 26%, and 39%, respectively. Although the selectivity of the Pd@VO<sub>2</sub> TFT sensor to methane is not satisfactory, the 50 ppm methane is far below the lower explosive limit, and the concentration of other interfering gases in the coal mine environment is even lower, so the Pd@VO<sub>2</sub> TFT sensor might show better and relatively ideal selectivity in practical applications. In addition, the Pd@VO<sub>2</sub> TFT sensor was stored in ambient air without power, and the sensor was discontinuously tested several times within 25 days, with each exposure being to 500 ppm CH<sub>4</sub> for 30 min. The long-term stability evaluation of the CH<sub>4</sub> sensor for 500 ppm CH<sub>4</sub> is shown in Figure 4f. It is clearly seen that the response value and initial current of the CH<sub>4</sub> sensor maintained excellent consistency without significant decay over 25 days. In addition, the moisture resistance of the sensor was further examined under different relative humidity values (0%, 10%, 30%, 50%, 70%, and 90%) at room temperature (data not shown). It was found that the humidity had a great influence on the sensor, especially when working at high humidity conditions, which

is a problem to be solved for the gas sensors currently operating at room temperature. We will focus on solving the inferior humidity resistance in future work.

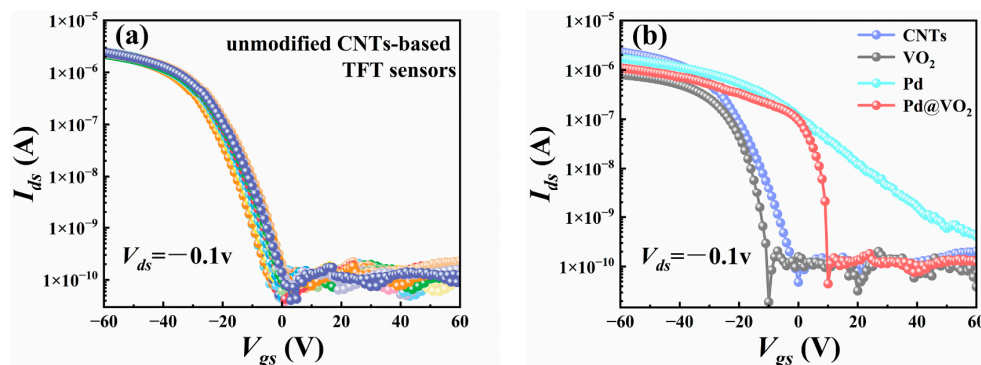


**Figure 3.** Electrical properties of TFT sensors. (a) Transfer characteristic curves of the randomly selected unmodified CNTs-based TFT sensors. (b) Comparison of transfer characteristic curves of VO<sub>2</sub>, Pd, and Pd@VO<sub>2</sub> TFT sensors with those of unmodified sensor.

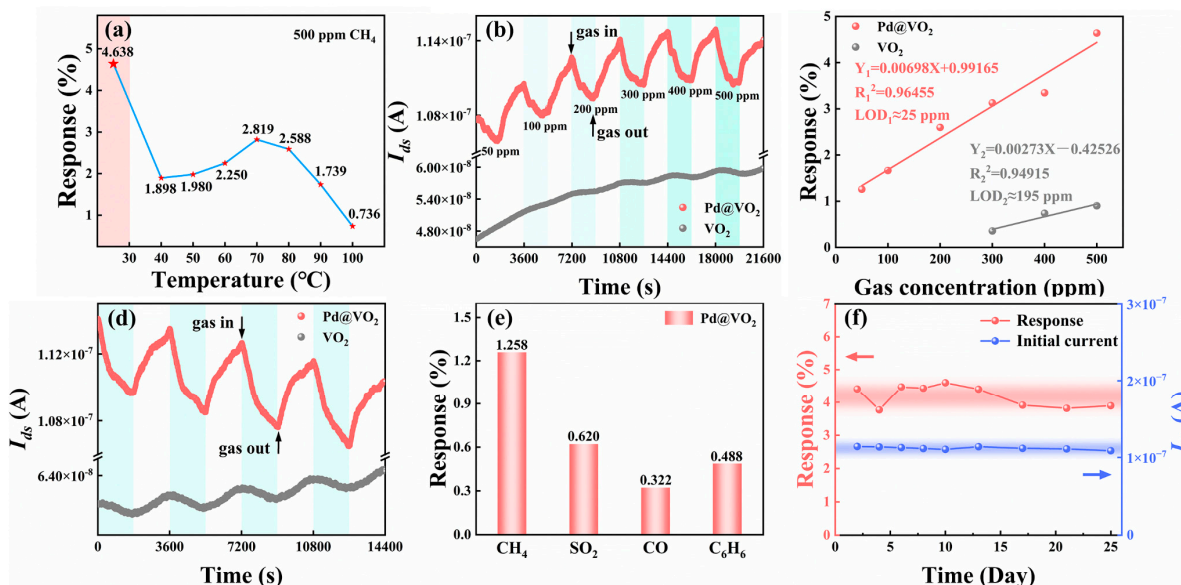
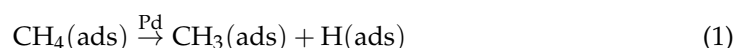


**Figure 4.** Gas-sensing properties of TFT sensors. (a) The response values of Pd@VO<sub>2</sub> TFT sensor toward 500 ppm CH<sub>4</sub> at different working temperatures. (b) The dynamic response–recovery curves, (c) the fitted curves, (d) the reproducibility test curves, and (e) the response values of Pd@VO<sub>2</sub> TFT sensor toward different gases at 50 ppm. (f) The response value and base current change in Pd@VO<sub>2</sub> TFT sensor measured several times within 25 days.

Based on the analysis of the above results, the main reason for the in of the gas sensitivity of the Pd@VO<sub>2</sub> TFT-type sensor may be attributed to the catalytic effect of Pd modification [2,50], which promotes the electronic interaction between CH<sub>4</sub> and gas-sensing materials and then regulates the CNTs’ electronic transmission channel. In addition, the inkjet printing method was used to make the sensitive material uniformly modify onto the surface of a CNT film, which is conducive to the uniform diffusion of gas molecules on a gas-sensing material surface [34]. The TFT gas-sensing platform based on CNTs modified by Pd@VO<sub>2</sub> is illustrated in Figure 5a. In air, the oxygen molecules adsorbed on the surface of VO<sub>2</sub> capture electrons from VO<sub>2</sub>-CNTs to form O<sub>2</sub><sup>-</sup> [51]. Therefore, the carriers of the p-type semiconductor CNTs increase instead, resulting in the widening of the conductive channel of the CNTs. In a CH<sub>4</sub> atmosphere, the generated electrons are released to VO<sub>2</sub>-CNTs due to the redox reaction between CH<sub>4</sub> molecules and oxygen ions, so that

the carriers of p-type semiconducting CNTs are reduced, resulting in the narrowing of the conductive channel of the CNTs. Due to the insufficient activation energy between the CH<sub>4</sub> and oxygen ions, the feeble redox reaction rate ultimately results in inferior gas-sensing properties of a sensor when operating at room temperature. It is noteworthy that Pd, as an active noble metal, can catalyze the dissociative adsorption of CH<sub>4</sub> and oxygen molecules via the spillover effect [52,53]. After the modification of Pd nanoparticles, Pd can promote the dissociation of oxygen molecules to produce oxygen atoms, which then spill over to the VO<sub>2</sub> surface and capture electrons from VO<sub>2</sub>-CNTs to form oxygen ions. The process can increase the adsorption amount of oxygen and the molecule-ion conversion rate of oxygen to provide more active sites for CH<sub>4</sub> gas (Figure 5b) [52]. In a CH<sub>4</sub> atmosphere, Pd can reduce the activation energy of the redox reaction between CH<sub>4</sub> and oxygen ions and can promote the dissociation of C-H bonds in CH<sub>4</sub> to form CH<sub>3</sub> and H [52]. The reaction is as follows [2]:



Subsequently, CH<sub>3</sub> and H spill onto the VO<sub>2</sub> surface and react with the preadsorbed oxygen ions to generate more free electrons (Figure 5c). The reaction is as follows [49]:



Finally, the CNTs' conductive channels become narrower, which leads to the improvement in the gas-sensing properties of Pd@VO<sub>2</sub> TFT sensors. In other words, the use of CNTs as the conductive channel of the TFT and the Pd@VO<sub>2</sub> composite as the sensitive layer of the sensor to capture CH<sub>4</sub> molecules seems to be the key factors to ultimately improving the gas-sensing properties of CNTs-based TFT gas sensors.

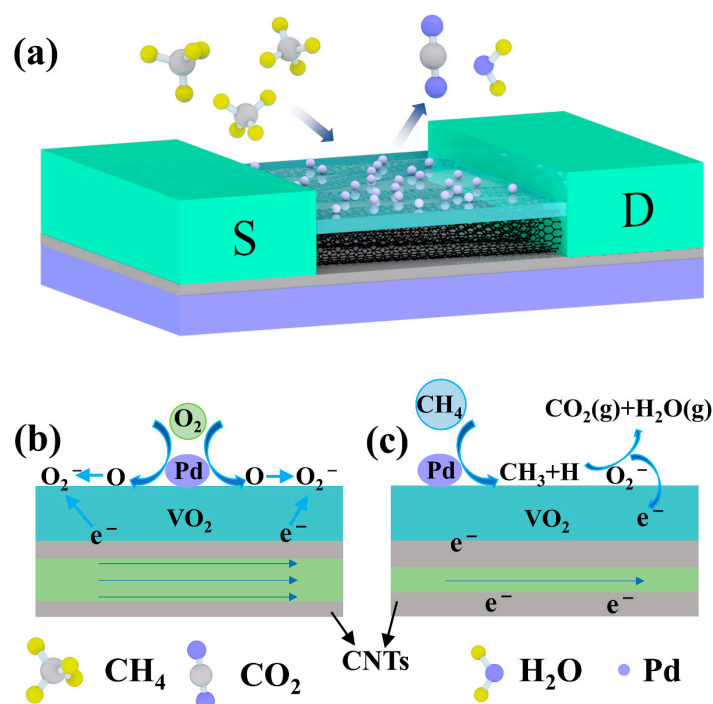


**Figure 5.** (a) Pd@VO<sub>2</sub> TFT gas-sensing platform based on CNTs. Schematic illustrations of the gas-sensing mechanisms (b) in air and (c) in CH<sub>4</sub> gas.

#### 4. Conclusions

In summary, a TFT-type gas sensor based on a CNT film was successfully fabricated by using semiconductor processing technology. Specifically, VO<sub>2</sub> material was deposited on the top of the semiconductor CNT channel via inkjet printing to achieve the detection of CH<sub>4</sub> at room temperature. Then, Pd nanoparticles as the catalyst were deposited onto the

surface of the VO<sub>2</sub> material; finally, the Pd@VO<sub>2</sub> TFT sensor showed better CH<sub>4</sub>-sensing properties. The response of the Pd@VO<sub>2</sub> TFT sensor toward 500 ppm CH<sub>4</sub> was about five times than that of the VO<sub>2</sub> TFT sensor under the same conditions, and the detection limit was optimized from 300 ppm to 50 ppm. The detection of CH<sub>4</sub> at room temperature could be attributed to the redox reaction of VO<sub>2</sub> nanomaterials, and the improvement in the gas-sensing performance of the Pd@VO<sub>2</sub> TFT sensor could be ascribed to the spillover effect of Pd nanoparticles. Our work provides a valuable reference for the low power consumption, miniaturization, and integrability of gas sensors, which opens a new window for the integration of high-performance micro gas sensors into electronic equipment.

**Supplementary Materials:** The following supporting information can be downloaded at: <https://www.mdpi.com/article/10.3390/chemosensors11070365/s1>, Figure S1: FE-SEM image of the CNTs. Figure S2: FE-SEM image of Pd@VO<sub>2</sub>, and the inset shows FE-SEM image at high magnification. Figure S3: EDS mapping of elements (a) V, (b) O, and (c) Pd. Figure S4: Two-cycle test of Pd-modified CNTs sensor for 500 ppm CH<sub>4</sub> at room temperature.

**Author Contributions:** Conceptualization, Y.Z.; methodology, F.J.; validation, F.J.; investigation, F.J.; writing—original draft preparation, F.J.; writing—review and editing, J.H. and Y.Z.; supervision, J.H. and Y.Z.; funding acquisition, J.H. and Y.Z. All authors have read and agreed to the published version of the manuscript.

**Funding:** This research was funded by National Natural Science Foundation of China, grant numbers 62071410 and 62101477; and the Hunan Provincial Natural Science Foundation of China, grant number 2021JJ40542.

**Institutional Review Board Statement:** Not applicable.

**Informed Consent Statement:** Not applicable.

**Data Availability Statement:** Data are available from the authors under reasonable request.

**Conflicts of Interest:** The authors declare no conflict of interest.

## References

1. Chimowa, G.; Tshabalala, Z.P.; Akande, A.A.; Bepete, G.; Mwakikunga, B.; Ray, S.S.; Benecha, E.M. Improving CH<sub>4</sub> gas sensing properties of multi-walled carbon nanotubes by vanadium oxide filling. *Sens. Actuators B Chem.* **2017**, *247*, 11–18. [[CrossRef](#)]
2. Wang, Y.; Meng, X.; Yao, M.; Sun, G.; Zhang, Z. Enhanced CH<sub>4</sub> sensing properties of Pd modified ZnO nanosheets. *Ceram. Int.* **2019**, *45*, 13150–13157. [[CrossRef](#)]
3. Liang, J.; Liu, J.; Li, N.; Li, W. Magnetron sputtered Au-decorated vanadium oxides composite thin films for CH<sub>4</sub>-sensing properties at room temperature. *J. Alloys Compd.* **2016**, *671*, 283–290. [[CrossRef](#)]
4. Liang, J.; Li, W.; Liu, J.; Hu, M. Room temperature CH<sub>4</sub> sensing properties of Au decorated VO<sub>2</sub> nanosheets. *Mater. Lett.* **2016**, *184*, 92–95. [[CrossRef](#)]
5. Kim, W.-T.; Kim, I.-H.; Choi, W.-Y. Fabrication of TiO<sub>2</sub> Nanotube Arrays and Their Application to a Gas Sensor. *J. Nanosci. Nanotechnol.* **2015**, *15*, 8161–8165. [[CrossRef](#)] [[PubMed](#)]
6. Zhang, Y.; Li, Y.; Liu, W.; Li, F.; Zhan, Z. Design of SnO<sub>2</sub>-based CH<sub>4</sub> sensors with reactive anti-poisoning layers: Excellent stability and high resistance to hexamethyldisiloxane. *J. Mater. Sci.* **2023**, *58*, 2140–2155. [[CrossRef](#)]
7. Sun, Y.; Hu, J.; Zhang, Y. Visible light assisted trace gaseous NO<sub>2</sub> sensor with anti-humidity ability via LSPR enhancement effect. *Sens. Actuators B Chem.* **2022**, *367*. [[CrossRef](#)]
8. Lu, G.; Ocola, L.E.; Chen, J. Room-Temperature Gas Sensing Based on Electron Transfer between Discrete Tin Oxide Nano-crystals and Multiwalled Carbon Nanotubes. *Adv. Mater.* **2009**, *21*, 2487–2491. [[CrossRef](#)]
9. Hu, J.; Liu, X.; Zhang, J.; Gu, X.; Zhang, Y. Plasmon-activated NO<sub>2</sub> sensor based on Au@MoS<sub>2</sub> core-shell nanoparticles with heightened sensitivity and full recoverability. *Sens. Actuators B Chem.* **2023**, *382*, 133505. [[CrossRef](#)]
10. Xiao, M.; Li, Y.; Zhang, B.; Sun, G.; Zhang, Z. Synthesis of g-C<sub>3</sub>N<sub>4</sub>-Decorated ZnO Porous Hollow Microspheres for Room-Temperature Detection of CH<sub>4</sub> under UV-Light Illumination. *Nanomaterials* **2019**, *9*, 1507. [[CrossRef](#)]
11. Xiao, M.; Liang, S.; Han, J.; Zhong, D.; Liu, J.; Zhang, Z.; Peng, L. Batch Fabrication of Ultrasensitive Carbon Nanotube Hydro-gen Sensors with Sub-ppm Detection Limit. *ACS Sens.* **2018**, *3*, 749–756. [[CrossRef](#)] [[PubMed](#)]
12. Liu, F.; Xiao, M.; Ning, Y.; Zhou, S.; He, J.; Lin, Y.; Zhang, Z. Toward practical gas sensing with rapid recovery semiconducting carbon nanotube film sensors. *Sci. China Inf. Sci.* **2022**, *65*, 162402. [[CrossRef](#)]
13. Abd, I.K.; Shano, A.M.; Khodair, Z.T. MWCNT Thin Films by CVD Method and Some Applications. *J. Nano-Electron. Phys.* **2022**, *14*, 06002. [[CrossRef](#)]

14. Shukla, P.; Saxena, P.; Madhwal, D.; Bhardwaj, N.; Jain, V.K. Electrostatically functionalized CVD grown multiwalled carbon nanotube/palladium polymer nanocomposite (MWCNT/Pd) for CH<sub>4</sub> detection at room temperature. *Chem. Eng. Sci.* **2022**, *264*, 118191. [[CrossRef](#)]
15. Lu, Y.; Li, J.; Han, J.; Ng, H.T.; Binder, C.; Partridge, C. Meyyappan, room temperature CH<sub>4</sub> detection using palladium loaded single-walled carbon nanotube sensors. *Chem. Phys. Lett.* **2004**, *391*, 344–348. [[CrossRef](#)]
16. Aroutiounian, V.M. Metal oxide gas sensors decorated with carbon nanotubes. *Lith. J. Phys.* **2015**, *55*, 4. [[CrossRef](#)]
17. Afrin, R.; Shah, N. Room temperature gas sensors based on carboxyl and thiol functionalized carbon nanotubes buckypapers. *Diam. Relat. Mater.* **2015**, *60*, 42–49. [[CrossRef](#)]
18. Humayun, T.; Divan, R.; Liu, Y.; Gundel, L.; Solomon, P.A.; Paprotny, I. Novel chemoresistive CH<sub>4</sub> sensor with 10 ppm sensitivity based on multiwalled carbon nanotubes functionalized with SnO<sub>2</sub> nanocrystals. *J. Vac. Sci. Technol. A* **2016**, *34*, 01A131. [[CrossRef](#)]
19. Humayun, M.T.; Divan, R.; Stan, L.; Gupta, A.; Rosenmann, D.; Gundel, L.; Solomon, P.A.; Paprotny, I. ZnO functionalization of multiwalled carbon nanotubes for CH<sub>4</sub> sensing at single parts per million concentration levels. *J. Vac. Sci. Technol. B Nanotechnol. Microelectron. Mater. Process. Meas. Phenom.* **2015**, *33*, 06FF01.
20. Chen, C.; Jiang, M.; Luo, X.; Tai, H.; Jiang, Y.; Yang, M.; Xie, G.; Su, Y. Ni-Co-P hollow nanobricks enabled humidity sensor for respiratory analysis and human-machine interfacing. *Sens. Actuators B Chem.* **2022**, *370*, 132441. [[CrossRef](#)]
21. Prasad, A.K.; Amirthapandian, S.; Dhara, S.; Dash, S.; Murali, N.; Tyagi, A.K. Novel single phase vanadium dioxide nanostructured films for CH<sub>4</sub> sensing near room temperature. *Sens. Actuators B Chem.* **2014**, *191*, 252–256. [[CrossRef](#)]
22. Li, W.; Liang, J.; Liu, J.; Zhou, L.; Yang, R.; Hu, M. Synthesis and room temperature CH<sub>4</sub> gas sensing properties of vanadium dioxide nanorods. *Mater. Lett.* **2016**, *173*, 199–202. [[CrossRef](#)]
23. Chen, Y.; Zhang, W.; Luo, N.; Wang, W.; Xu, J. Defective ZnO Nanoflowers Decorated by Ultra-Fine Pd Clusters for Low-Concentration CH<sub>4</sub> Sensing: Controllable Preparation and Sensing Mechanism Analysis. *Coatings* **2022**, *12*, 677. [[CrossRef](#)]
24. Li, S.; Huang, H.; Zhao, D. GaN Nanowires Decorated with Pd for CH<sub>4</sub> Gas Sensor. In *IOP Conference Series: Earth and Environmental Science*; IOP Publishing: Bristol, UK, 2020; p. 042037.
25. Luo, S.; Chen, R.; Wang, J.; Xiang, L. ZnO/Pd@ ZIF-7-Based Gas Sensors for Selective CH<sub>4</sub> Sensing. *ACS Appl. Nano Mater.* **2023**, *67*, 5808–5816. [[CrossRef](#)]
26. Liu, C.; Hu, J.; Wu, G.; Cao, J.; Zhang, Z.; Zhang, Y. Carbon Nanotube-Based Field-Effect Transistor-Type Sensor with a Sensing Gate for Ppb-Level Formaldehyde Detection. *ACS Appl. Mater. Interfaces* **2021**, *13*, 56309–56319. [[CrossRef](#)]
27. Kim, C.-H.; Cho, I.-T.; Shin, J.-M.; Choi, K.-B.; Lee, J.-K.; Lee, J.-H. A New Gas Sensor Based on MOSFET Having a Horizontal Floating-Gate. *IEEE Electron Device Lett.* **2013**, *35*, 265–267. [[CrossRef](#)]
28. Hong, Y.; Kim, C.-H.; Shin, J.; Kim, K.Y.; Kim, J.S.; Hwang, C.S.; Lee, J.-H. Highly selective ZnO gas sensor based on MOSFET having a horizontal floating-gate. *Sens. Actuators B Chem.* **2016**, *232*, 653–659. [[CrossRef](#)]
29. Liang, Y.; Xiao, M.; Wu, D.; Lin, Y.; Liu, L.; He, J.; Zhang, G.-J.; Peng, L.-M.; Zhang, Z. Wafer-Scale Uniform Carbon Nanotube Transistors for Ultrasensitive and Label-Free Detection of Disease Biomarkers. *ACS Nano* **2020**, *14*, 8866–8874. [[CrossRef](#)]
30. Zhou, S.; Xiao, M.; Liu, F.; He, J.; Lin, Y.; Zhang, Z. Sub-10 parts per billion detection of hydrogen with floating gate transistors built on semiconducting carbon nanotube film. *Carbon* **2021**, *180*, 41–47. [[CrossRef](#)]
31. Franco, M.A.; Conti, P.P.; Andre, R.S.; Correa, D.S. A review on chemiresistive ZnO gas sensors. *Sens. Actuators Rep.* **2022**, *4*, 100100. [[CrossRef](#)]
32. Huang, Y.; Guo, J.; Kang, Y.; Ai, Y.; Li, C.M. Two dimensional atomically thin MoS<sub>2</sub> nanosheets and their sensing applications. *Nanoscale* **2015**, *7*, 19358–19376. [[CrossRef](#)]
33. Biswas, C.; Lee, S.Y.; Ly, T.H.; Ghosh, A.; Dang, Q.N.; Lee, Y.H. Chemically Doped Random Network Carbon Nanotube p-n Junction Diode for Rectifier. *ACS Nano* **2011**, *5*, 9817–9823. [[CrossRef](#)]
34. Peng, X.; Liu, J.; Tan, Y.; Mo, R.; Zhang, Y. A CuO thin film type sensor via inkjet printing technology with high reproducibility for ppb-level formaldehyde detection. *Sens. Actuators B Chem.* **2022**, *362*, 131775. [[CrossRef](#)]
35. Braun, F.; Tarditi, A.M.; Miller, J.B.; Cornaglia, L.M. Pd-based binary and ternary alloy membranes: Morphological and permselective characterization in the presence of H<sub>2</sub>S. *J. Membr. Sci.* **2014**, *450*, 299–307. [[CrossRef](#)]
36. Alie, D.; Gedvilas, L.; Wang, Z.; Tenent, R.; Engtrakul, C.; Yan, Y.; Shaheen, S.E.; Dillon, A.C.; Ban, C. Direct synthesis of thermochromic VO<sub>2</sub> through hydrothermal reaction. *J. Solid State Chem.* **2014**, *212*, 237–241. [[CrossRef](#)]
37. Kong, F.; Li, M.; Pan, S.; Zhang, Y.; Li, G. Synthesis and thermal stability of W-doped VO<sub>2</sub> nanocrystals. *Mater. Res. Bull.* **2011**, *46*, 2100–2104. [[CrossRef](#)]
38. Chen, L.; Ruan, Y.; Zhang, G.; Wei, Q.; Jiang, Y.; Xiong, T.; He, P.; Yang, W.; Yan, M.; An, Q.; et al. Ultrastable and High-Performance Zn/VO<sub>2</sub> Battery Based on a Reversible Single-Phase Reaction. *Chem. Mater.* **2019**, *31*, 699–706. [[CrossRef](#)]
39. Li, R.; Liu, C.-Y. VO<sub>2</sub>(B) nanospheres: Hydrothermal synthesis and electrochemical properties. *Mater. Res. Bull.* **2010**, *45*, 688–692. [[CrossRef](#)]
40. Lee, S.-H.; Cheong, H.M.; Seong, M.J.; Liu, P.; Tracy, C.; Mascarenhas, A.; Pitts, J.; Deb, S.K. Raman spectroscopic studies of amorphous vanadium oxide thin films. *Solid State Ion.* **2003**, *165*, 111–116. [[CrossRef](#)]
41. Silversmit, G.; Depla, D.; Poelman, H.; Marin, G.B.; De Gryse, R. Determination of the V2p XPS binding energies for different vanadium oxidation states (V5+ to V0+). *J. Electron Spectrosc. Relat. Phenom.* **2004**, *135*, 167–175. [[CrossRef](#)]
42. Brun, M.; Berthet, A.; Bertolini, J. XPS, AES and Auger parameter of Pd and PdO. *J. Electron Spectrosc. Relat. Phenom.* **1999**, *104*, 55–60. [[CrossRef](#)]

43. Powell, M.J.; Godfrey, I.J.; Quesada-Cabrera, R.; Malarde, D.; Teixeira, D.; Emerich, H.; Palgrave, R.G.; Carmalt, C.J.; Parkin, I.P.; Sankar, G. Qualitative XANES and XPS Analysis of Substrate Effects in VO<sub>2</sub> Thin Films: A Route to Improving Chemical Vapor Deposition Synthetic Methods? *J. Phys. Chem. C* **2017**, *121*, 20345–20352. [[CrossRef](#)]
44. Luo, M.; Zhu, M.; Wei, M.; Shao, S.; Robin, M.; Wei, C.; Cui, Z.; Zhao, J.; Zhang, Z. Radiation-hard and repairable complementary metal–oxide–semiconductor circuits integrating n-type indium oxide and p-type carbon nanotube field-effect transistors. *ACS Appl. Mater. Interfaces* **2020**, *12*, 49963–49970. [[CrossRef](#)] [[PubMed](#)]
45. Zhang, Z.; Wang, S.; Ding, L.; Liang, X.; Pei, T.; Shen, J.; Xu, H.; Chen, Q.; Cui, R.; Li, Y.; et al. Self-Aligned Ballistic n-Type Single-Walled Carbon Nanotube Field-Effect Transistors with Adjustable Threshold Voltage. *Nano Lett.* **2008**, *8*, 3696–3701. [[CrossRef](#)]
46. Xu, X.; He, X.; Wang, G.; Yuan, X.; Liu, X.; Huang, H.; Chu, J. The study of optimal oxidation time and different temperatures for high quality VO<sub>2</sub> thin film based on the sputtering oxidation coupling method. *Appl. Surf. Sci.* **2011**, *257*, 8824–8827. [[CrossRef](#)]
47. Bertrand, J. Spectroscopic and Electrical Studies of the Influence of Electrodes on SnO<sub>2</sub> Based Sensors. Ph.D. Thesis, Tübingen, Univ., Tübingen, Germany, 2008.
48. Liu, J.; Hu, Z.; Zhang, Y.; Li, H.-Y.; Gao, N.; Tian, Z.; Zhou, L.; Zhang, B.; Tang, J.; Zhang, J.; et al. MoS<sub>2</sub> Nanosheets Sensitized with Quantum Dots for Room-Temperature Gas Sensors. *Nano-Micro Lett.* **2020**, *12*, 219–242. [[CrossRef](#)]
49. Kim, S.-J.; Hwang, I.-S.; Kang, Y.C.; Lee, J.-H. Design of Selective Gas Sensors Using Additive-Loaded In<sub>2</sub>O<sub>3</sub> Hollow Spheres Prepared by Combinatorial Hydrothermal Reactions. *Sensors* **2011**, *11*, 10603–10614. [[CrossRef](#)] [[PubMed](#)]
50. Horastani, Z.K.; Sayedi, S.M.; Sheikhi, M.H.; Rahimi, E. Effect of silver additive on electrical conductivity and CH<sub>4</sub> sensitivity of SnO<sub>2</sub>. *Mater. Sci. Semicond. Process.* **2015**, *35*, 38–44. [[CrossRef](#)]
51. Mounasamy, V.; Mani, G.K.; Madanagurusamy, S. Vanadium oxide nanostructures for chemiresistive gas and vapour sensing: A review on state of the art. *Microchim. Acta* **2020**, *187*, 253. [[CrossRef](#)]
52. Nasresfahani, S.; Sheikhi, M.; Tohidi, M.; Zarifkar, A. CH<sub>4</sub> gas sensing properties of Pd-doped SnO<sub>2</sub>/reduced graphene oxide synthesized by a facile hydrothermal route. *Mater. Res. Bull.* **2017**, *89*, 161–169. [[CrossRef](#)]
53. Liu, C.; Suematsu, K.; Uchiyama, A.; Watanabe, K.; Guo, Y.; Wang, D.; Shimano, K. Impact of Pd nanoparticle loading method on SnO<sub>2</sub> surface for natural gas detection in humid atmosphere. *J. Mater. Sci.* **2021**, *56*, 13975–13988. [[CrossRef](#)]

**Disclaimer/Publisher’s Note:** The statements, opinions and data contained in all publications are solely those of the individual author(s) and contributor(s) and not of MDPI and/or the editor(s). MDPI and/or the editor(s) disclaim responsibility for any injury to people or property resulting from any ideas, methods, instructions or products referred to in the content.